Self-Powered Miniaturized Acceleration Sensor Based on Rationally Patterned Electrodes

BAOCHENG WANG[1,2], XUELIAN WEI[1,2], JUNHUAN CHEN[1], ZHIHAO YUAN[1], YAPENG SHI[1,2], ZHIYI WU ⓘ[1,3], AND ZHONG LIN WANG[1,4]

[1] Beijing Institute of Nanoenergy and Nanosystems, Chinese Academy of Sciences, Beijing 100083, China
[2] College of Nanoscience and Technology, University of Chinese Academy of Science, Beijing 100049, China
[3] CUSPEA Institute of Technology, Wenzhou, Zhejiang 325024, China
[4] School of Materials Science and Engineering, Georgia Institute of Technology, Atlanta, GA 30332 USA

CORRESPONDING AUTHORS: ZHIYI WU AND ZHONG LIN WANG (e-mail: wuzhiyi@binn.cas.cn; zhong.wang@mse.gatech.edu).

ABSTRACT Acceleration sensors have a wide variety of applications for industrial engineering, biology and navigation. However, passive sensing, narrow detection range, large size, and high manufacturing cost curb their further development. Here, we present a miniaturized acceleration sensor (MAS) with rationally patterned electrodes, based on the single electrode triboelectric mechanism, featuring small size, high accuracy, large detection scale, and environmental friendliness. A stainless-steel ball, as the moving part of the MAS, experiences physical movement that is converted into an electrical signal. Equipped with rationally patterned electrodes, the MAS retains the smallest size and lowest weight compared with the currently reported self-powered acceleration sensors. Benefiting from the voltage-relationship-based direction detection mechanism, eight directions can be identified by one TENG module. Consequently, rotated 22.5° relatively, two TENG modules enable the MAS to detect 16 directions. Moreover, accelerations ranging from 0.1 m/s^2 to 50 m/s^2 can be identified according to the relationship of response time and accelerations in the horizontal direction. The relationship is obtained through the measurements of the sum of output voltages (V_{SOC}) for the four bottom electrodes with varying accelerations. In addition, no distinct decrease of V_{SOC} is observed after continuously operating for 2000 circles, presenting excellent robustness. Hence, this cost-effective and rationally patterned MAS reveals great potential for human machine interaction, VR/AR (virtual/augmented reality), sports training, and smart city.

INDEX TERMS Acceleration sensor, triboelectric nanogenerator, miniaturization, smart device.

I. INTRODUCTION

Acceleration sensors play a critical role in various fields of industry and science, for example, automotive industry, health-care monitoring, consumer electronics, and structural monitoring [1]–[4]. The commonly adopted mechanisms include capacitive [5]–[6], piezoresistive [7]–[8], and piezoelectric [9]–[10] mechanisms. However, some of these technologies expose several limitations, for instance, both of capacitive and piezoresistive acceleration sensors struggle to simplify their structures because they have to carry batteries. As for piezoelectric ones, the voltage signals are too small to be detected, thus limiting the further enhancement of sensitivity.

Therefore, a facile, optimized, and battery-free technology is highly desired.

Recently, based on the coupling of contact electrification and electrostatic induction, triboelectric nanogenerators (TENGs) that can convert various ambient mechanical motions into electricity, are emerging in both energy supply [11]–[17] and self-powered sensing [18]–[25]. TENGs are eminently suitable to be utilized to fabricate acceleration sensors, featuring lightweight, flexibility, and low cost, as well as having a wide selection of possible materials [26]–[27]. However, although a variety of acceleration sensors based on TENGs were reported, the small detection range, large size

and weight hinder their commercial applications, as shown in Table S1.

Triboelectric acceleration sensors are basically composed of a static part and moving part [28]–[30]. In the process of acceleration, the acceleration value is obtained by measuring the inertia force applied on the mass directly or indirectly, according to Newton's second law. Zhang et al. selected a mercury drop, a kind of liquid metal mercury, as the moving part owing to its high elasticity [19]. Nevertheless, it is harmful to the environment and has a smaller contact angle compared with a solid ball, which may attenuate the sensitivity of an acceleration sensor. Image deleted. Please check.

Consequently, a mass possessing low toxicity and larger contact angles is a more appropriate choice. As for the static part, the design of electrode patterns is the key point to simplify the structure of an acceleration sensor. Pang et al. developed a 3D acceleration sensor based on three TENGs perpendicular with each other to determine accelerations [31], but it is not able to take full advantage of the voltage relationship of electrodes, resulting in the low integration of the sensor. Therefore, designing a rational electrode pattern is significant to facilitate the miniaturization of an acceleration sensor. The acceleration sensor developed by Zhang et al. is based on a coded strategy of electrodes [19]. Yet five circles of electrodes are required to realize the identification of accelerations, leading to the large diameter of the sensor. Moreover, a triboelectric interface that is able to identify finger sliding trajectory with only four electrodes was developed which can simplify the electrode pattern effectively. Besides, it detects the direction of objects based on the voltage relationships of adjacent electrodes, enabling it to avoid the influences of the variations of temperature and humidity [32]. In addition, the sum of output voltages (V_{SOC}) for the four bottom electrodes can be utilized to measure the accelerations applied to a sensor. Consequently, equipped with the electrode pattern, the sensor is capable of detecting the directions and magnitudes of accelerations imposed on the sensor.

Herein, a rationally patterned miniaturized acceleration sensor (MAS), based on single electrode triboelectric mechanism, is developed, featuring small size, high accuracy, large detection scale, and environmental friendliness. A stainless-steel ball functions as the moving part of the MAS, experiencing physical movement that is converted into an electrical signal. The volume and weight of the sample for the MAS are only 1.27 cm^3 and 0.87 g, respectively, with its diameter of 16.91 mm and height of 6.31 mm (Fig. S2). It is the smallest self-powered acceleration sensor compared with previously reported ones (Table S1), on account of its simple configuration. (Fig. S1(b)). The MAS differentiates directions through the voltage relationships of adjacent electrodes, thus presenting excellent precision. The MAS is able to detect 16 directions benefiting from two TENG modules rotated 22.5° relatively, the strategy of which effectively miniaturizes the acceleration sensor on the premise of not hampering the accuracy of direction detection. V_{SOC} of the four bottom electrodes is used to investigate the relationship of accelerations and response time. The MAS can response to accelerations ranging

from 0.1 m/s^2 to 50 m/s^2 according to the relationship. Therefore, the rationally patterned, low-cost and environmentally friendly MAS reveals its great potential for human machine interaction, VR/AR (virtual/augmented reality), sports training, smart home, and smart city.

II. RESULTS AND DISCUSSIONS

The structure diagram and entity of the MAS are demonstrated in Fig. 1(a) and Fig. S1(b), respectively. The bone of the MAS mainly consists of a cylinder-shaped plate, a ring-shaped plate and a hemisphere-shaped plate which are all made of acrylic. The shape of the bottom plate surface is concave, the slope of which is approximately 16.4°, the fabrication process, the calculation, and the entity of which are illustrated in Fig. S3(a), Fig. S3(b), and Fig. 1(c), respectively. Four copper electrodes are deposited on the bottom plate (Fig. 1(c)) and the copper electrodes attached on the top plate are of same shape with the bottom ones (Fig. S1). Each of the eight copper electrodes is onImage deleted. Please check. eighth annulus with inner diameter of 7 mm and outer diameter of 10 mm. The diagram in Fig. 1(b) illustrates that the top copper electrodes are rotated 22.5° relative to the bottom copper electrodes which enable the sensor to detect 16 accelerations precisely. The PTFE films are directly covered on the two acrylic substrates with electrodes, serving as the negative triboelectric layer. Due to its strong electronic attraction, PTFE is easy to gain electrons from almost any other materials. The root cause is that PTFE has high density fluorine group which endows it with strong electronegativity. There will be friction between the ball and two PTFE films when an external stimulation is applied to the MAS. Besides, the stainless-steel ball forms the positive triboelectric layer. Therefore, the MAS can be divided into the top TENG module and the bottom TNEG module which have a common positive triboelectric dielectric. Since the operation mechanism of the bottom and top TENG modules are generally identical, both based on single-electrode mode triboelectric nanogenerators, the bottom TENG module is adopted to elucidate the operation mechanism as shown in Fig. 1(d). The left electrode is BE1, and the right electrode is BE3. The moving track of the ball in Fig. 1(d) is just the central connection of BE1 and BE3. The whole process of working mechanism can be separated into four states. Owing to the different affinities to electrons, the PTFE layer become negatively charged and the stainless ball become positively charged on their surfaces after contacting with each other based on contact electrification. After a few circles, the charges on their surfaces will be saturated and cannot be neutralized. The electric potential between the copper electrodes and the ground are equivalent (i). Next, as the ball moves from the BE1 to the center of two electrodes, the electrostatic balance is broken and thus electrons will be repelled from the ground to BE3 in the external circuit by the electric potential difference, based on the electrostatic induction. For BE1, the flow of electrons is the reverse of BE2 (ii). The electrostatic balance is established again (iii). When the ball moves from BE3 to the center of two electrodes, the flow of electrons of
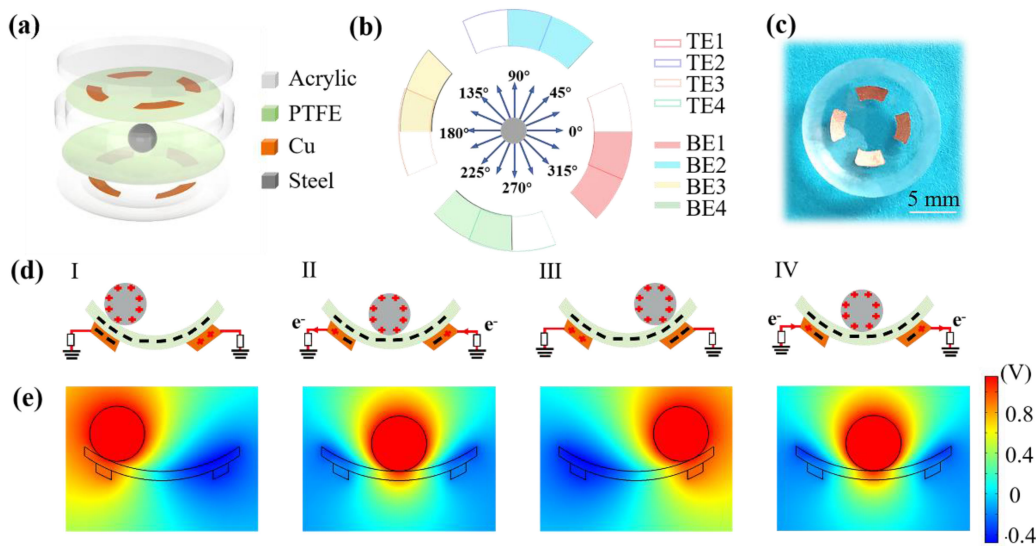
FIGURE 1. Structural design and working principle of the MAS. (a) Schematic illustration of the MAS. (b) The relative position of eight copper electrodes deposited on the top and bottom plates. (c) Digital photograph of the copper electrodes deposited on the lower acrylic plate. Scale bar, 5 mm. (d) Working mechanism of the MAS. (e) Potential distribution between the stainless-steel ball, the PTFE film with the ball moving from BE1 to BE3.
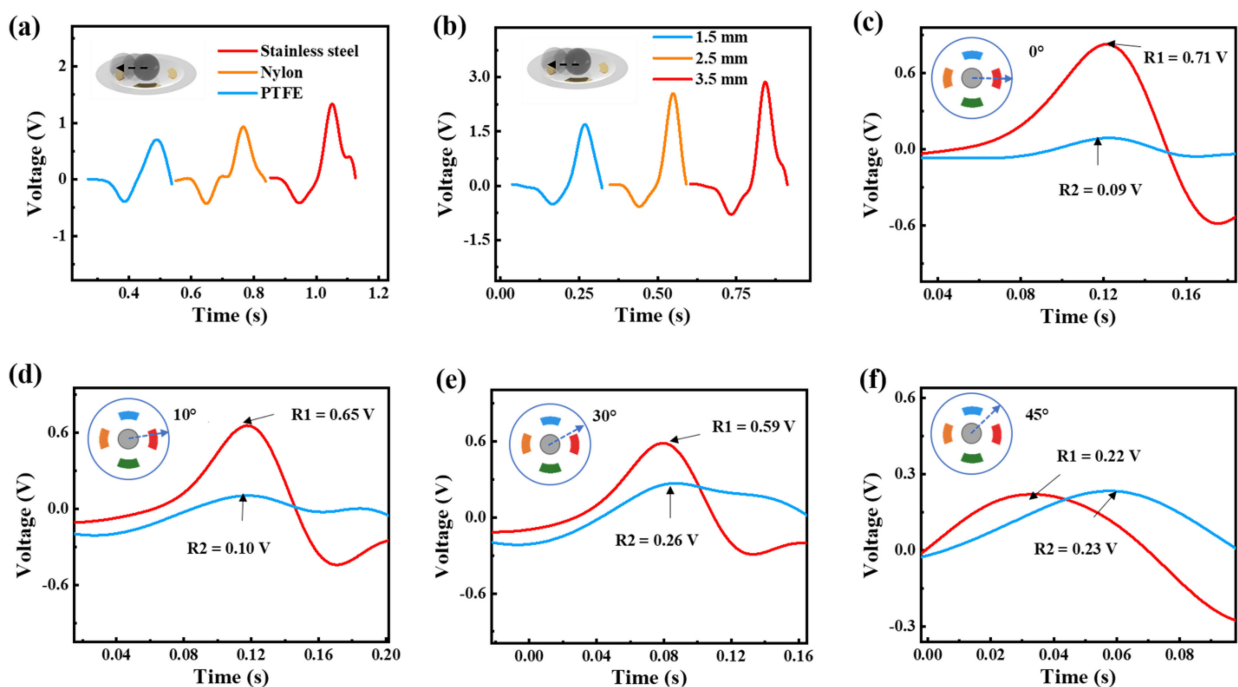

FIGURE 2. Material selection and the structure design of the MAS. (a) VOC generated by different types of ball (Stainless steel, PTFE, and Nylon) moving across the copper electrode BE1. Insets show the moving directions of the ball. (b) VOC of the electrode width ranging from 1.5 mm, 2.5 mm to 3.5 mm. Insets show the moving directions of the ball. (c-f) VOC of TE1 and TE2. Insets show the moving directions of the ball and the solid circle represents the upper acrylic substrate whereas the dotted circle represents the lower acrylic substrate.

BE1 and BE3 are quite the opposite of state ii (iv), until a new balance is achieved (i). As a result, alternating voltages signals can be obtained. The static and dynamic potential distribution of the process mentioned above is simulated by COMSOL, as illustrated in Fig. 1(e) and Supporting Movie.

The material selection of the moving part for the MAS is vital to its performance such as accuracy, response velocity, and robustness. Consequently, the materials possessing low toxicity and larger contact angles are investigated in this work in order to select a more suitable material. The effect of material selection on the output voltage of the bottom and top TENG modules are demonstrated in Fig. 2(a) and Fig. S4(a). The magnitude of voltage peak values decreases with the order of stainless steel, nylon, and PTFE for both BE1 and
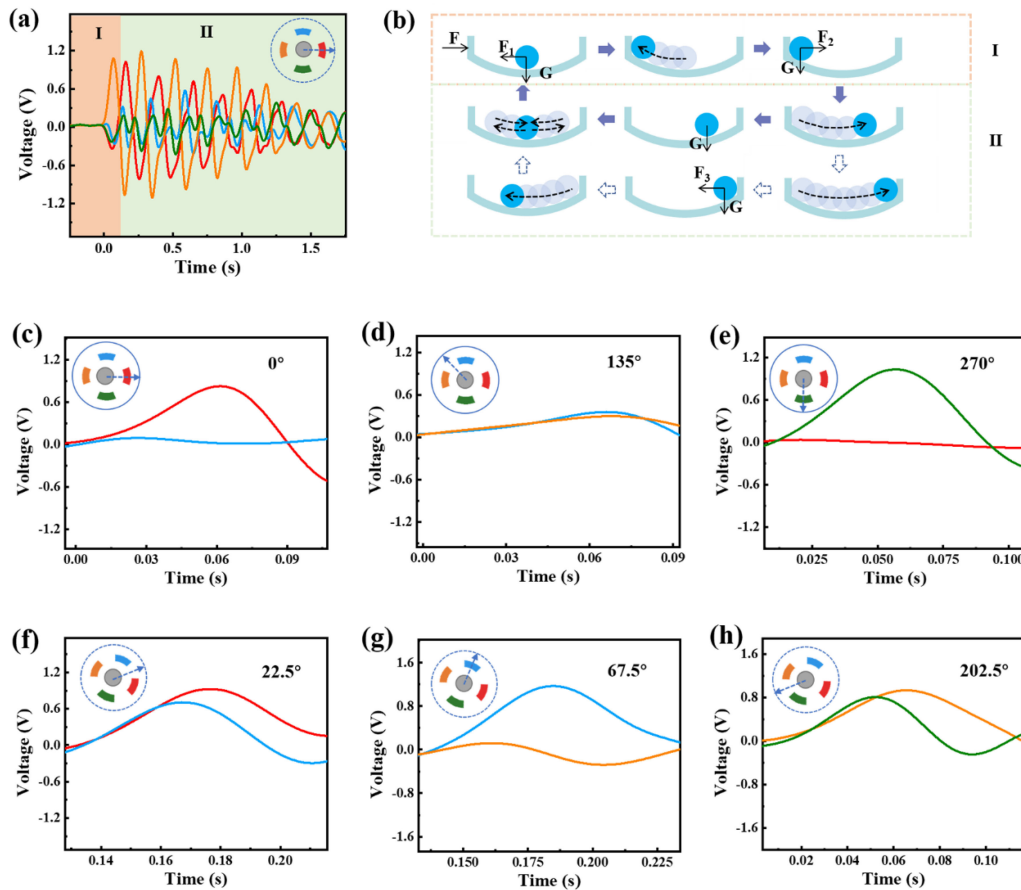
FIGURE 3. Direction detection of the MAS in the horizontal plane. (a) V_{OC} of BE1-BE4 when a specific force applied to the sensor in the direction as shown in the inset. (b) Force and movement analysis of the stainless-steel ball when an external stimulation is applied to the MAS. (c–h) V_{OC} of six directions. Insets show the moving directions of the ball and the solid circle represents the upper acrylic substrate whereas the dotted circle represents the lower acrylic substrate.

TE1. The ball made of PTFE has an identical triboelectric polarity with the PTFE film pasted on copper electrodes, which makes it unsuitable to be chosen as the positive triboelectric dielectric of the MAS. As for stainless steel and nylon, stainless steel is more likely to lose electrons based on the triboelectric sequence [34]. In addition, the density of a stainless-steel ball is larger than nylon ball, enabling it to move along the direction of an external force applied to the sensor accurately. Thereby a stainless-steel ball is determined as the moving part of the MAS. Moreover, the ball size can influence V_{OC} of the MAS, which is illustrated in Fig. S4(b-c). A larger V_{OC} can Image deleted. Please check. be obtained from a larger diameter for both TE1 and BE1. The V_{OC} of 3 mm ball is large enough to satisfy the sensing requirements of the MAS. Consequently, the 3 mm ball is selected, which is advantageous to minimize the size of the MAS. Measurements of transferred charge are conducted as shown in Fig. S4(d). The transferred charge increases with the increase of diameter because a larger contact area between the ball and PTFE can enhance the quantity of transferred charges. The frequency response of MAS 's output performance is shown in Fig. S6. Both the voltage and transferred charge of BE1 present an

increase with the enhancement of frequency in the horizontal direction.

With respect to the design of electrode patterns, it is crucial that heightening the precision of the MAS and reducing its electrode size as much as possible on the premise of not hampering the function of the MAS. The basic strategy of detecting directions in the horizontal plane is based on V_{OC} relationships of adjacent electrodes. Measurements of variable electrodes with ring width ranging from 1.5 mm, 2.5 mm, 3.5 mm are conducted as shown in Fig. 2(b). It is observed that larger V_{OC} can be obtained from the larger ring width, indicating that the ball moves across the larger electrode area, the larger V_{OC} can be generated. The results demonstrate the feasibility of the direction detecting strategy from the perspective of theory. Besides, the V_{OC} of 1.5 mm is large enough to detect the direction thus the ring width of 1.5 mm is selected.

Furthermore, the accuracy of the direction detection is demonstrated in Fig. 2(c–f) and insets show the moving directions of the ball. The solid circle represents the top acrylic substrate and the dotted circle represents the bottom acrylic substrate. It is observed that the V_{OC} of TE1 achieves its maximum at 0°, whereas the V_{OC} of TE2 achieves its minimum.
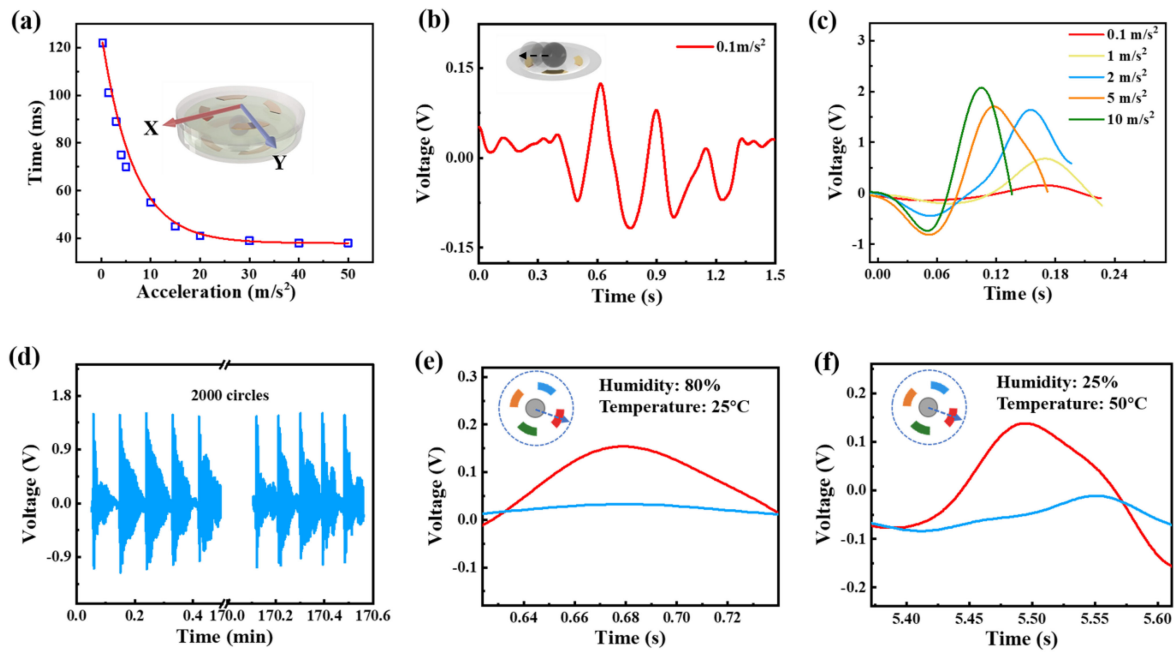
FIGURE 4. Acceleration measurements of the MAS in the horizontal direction. (a) Relationship of the response time (from the first trough to the first peak) and magnitudes of acceleration. (b) V_{SOC} of the four bottom electrodes waveform under 0.1 m/s². (c) V_{SOC} of the four bottom electrodes under 0.1 m/s², 1 m/s², 2 m/s², 5 m/s² and 10 m/s². (d) V_{SOC} of the four bottom electrodes after continuous operation for 2000 circles under 2 m/s². (e) V_{OC} of BE1 and BE2 at 2 m/s² when the humidity and temperature are 80% and 25°C, respectively. The inset shows the moving directions of the ball. (f) V_{OC} of BE1 and BE2 at 2m/s² when the humidity and temperature are 25% and 50°C, respectively. The inset shows the moving directions of the ball.

The V_{OC} of TE1 and TE2 become the same approximately at 45° (Fig. 2(f)). Moreover, the V_{OC} of TE1 decreases and the V_{OC} of TE2 increases with directions ranging from 0°, 10°, 30° to 45° (Fig. 2(c–f)), demonstrating the good accuracy of direction detecting. Similarly, the same changing tendency can be observed in Fig. S4(e-h). The explanations of Fig. 2(c–f) are as follows. The ball moves across the smaller electrode area of TE1 when directions vary from 0°, 10°, 30° to 45°, whereas it moves across the larger electrode area of TE2. Hence, the varying tendency in Fig. 2(c–f) can be clarified.

However, the voltage ratios of adjacent electrodes at 10° and 30° are not as stable as those at 0° and 45°. And the waveforms at 0° and 45° are more distinguishable in comparison with those at 10° and 30°. As a result, the MAS can accurately detect 0° and 45° compared with 10° and 30°. Since the electrodes pattern is centrosymmetric, one TENG module can detect eight directions. Therefore, if the top TENG module is rotated 22.5° corresponding to the bottom TENG module, 16 directions can be precisely identified by the whole sensor. The schematic diagram of 16 directions detected by the two staggered TENG modules is demonstrated in Fig. 1(b). We believe that the accuracy of the MAS can be enhanced in the future work through further investigation of the relationship between the accuracy and electrode patterns.

The moving process of the ball is illustrated in Fig. 3(b) and corresponding V_{OC} waveform can be separated into two stages as shown in Fig. 3(b) and Fig. S5(a) When an external force (F) is applied to the MAS, due to the inherent inertia of the ball, the ball slides toward the opposite direction of the external force relative to the substrate until it knocks the acrylic

ring (stage I). After that, the ball moves along the direction of F under G (gravity) and F1 (thrust). If the magnitude of F is small, the ball will swing at the bottom under G and F2 until it is finally still at the center of the bottom substrate. In the other case, the ball will knock the acrylic ring again and will not stop under G and F3 until it slows down (stage II). The first peak of the waveform in Fig. 3(a) is chosen to identify the direction since its corresponding moving direction of the ball is the same as F. Measurements of the V_{OC} at six directions are illustrated in Fig. 3(c–h). The other directions are demonstrated in Fig. S5. Therefore, each TENG module can detect eight directions. It can be observed that the V_{OC} of electrodes at the bottom substrate are larger than that of electrodes at the top substrate in general. For instance, the V_{OC} of E1 at 337.5° is larger than that of E5 at 0°. The reason is that the contact area between the ball and the bottom electrode is larger than that of the top electrode. Moreover, the ball exerts more pressure on the bottom electrodes than on the top electrode. As a result, a larger V_{OC} is obtained from the bottom electrode, whereas a smaller V_{OC} is achieved from the top electrode when the acceleration is the same. However, the result does not affect the direction detection of the top TENG module since that the direction mechanism is based on the voltage relationship of adjacent electrodes, which is demonstrated in Fig. 3(c–e) and Fig. S5 (d-g, j). In the assembling of the MAS, the top TENG module is rotated 22.5° anticlockwise corresponding to the bottom TENG module, which enables the MAS to detect 16 directions based on this ingenious structure. Besides, this structure is advantageous to minimize the size of the MAS, which facilitates the

application of the MAS on VR/AR, sports training, smart home and smart city. It is concluded that the MAS is able to detect 16 directions precisely.

The dependence of response time (defined as the time from the first trough to the first peak of output waveforms) on accelerations ranging from 0.1 m/s^2 to 50 m/s^2 are illustrated in Fig. 4(a). V_{SOC} of the four bottom electrodes is utilized to investigate this relationship, the results of which is applicative to all directions in the horizontal plane because the relationship is irrelevant to the magnitude of V_{SOC}. As a result, another electrode used to detect accelerations is no longer required based on this strategy. Apparently, the response time is in negative exponential relationship with acceleration. Besides, the experimental data is fixed well with the fitting curve. Furthermly, the sensor has great sensitivity in low accelerations region as shown in Fig. 4(b). Even though the acceleration is as low as 0.1 m/s^2, the magnitude of V_{SOC} can achieve 0.12 V, which is significant in identification of mild vibration. The range of acceleration detection can be changed by adjusting the arc at the bottom of the sensor. Decreasing the slope can reduce the resistance of the moving ball, which may be advantageous to detection of the low acceleration, such as a mild vibration. On the contrary, increasing the slope will attenuate the detection ability of the MAS at low acceleration and broaden the detection range at high acceleration. Consequently, there is no linear relationship between the slope and acceleration detection range, which may be addressed in the future work. Measurements of V_{SOC} under different accelerations are conducted, the details of which is illustrated in Fig. 4(c). Obviously, with the increasing accelerations, the peak values are enhancing whereas the response time is decreasing. Moreover, V_{SOC} of the sensor is stable, which maintains the same amplitude after 2000 circles as shown in Fig. 4(d). The MAS presents good thermal and moist stability. Although the V_{OC} decreases at 50°C and 80%, the MAS can still detect 337.5° at 50°C and 80% air humidity, respectively, based on the V_{OC} relationship between BE1 and BE2, which is demonstrated in Fig. 4(e-f). The relationship between adjacent electrodes is distinguishable. Thus the MAS can still realize its function at 50°C and 80% air humidity, respectively.

III. CONCLUSION

In summary, a rationally patterned MAS is achieved with features of small size, high accuracy, large detection scale and environmental friendliness based on single electrode triboelectric mechanism. The volume and weight of the sample in Fig. S2 are only 1.27 cm^3 and 0.87 g, respectively, which facilitates its application in smart devices. Through material optimization, a stainless-steel ball is determined as the moving part of the MAS. After systematic and detailed measurements, the MAS is demonstrated to identify 16 directions with the aid of two TENG modules staggered by 22.5°. Moreover, the MAS is able to detect acceleration ranging from 0.1 m/s^2 to 50 m/s^2, presenting high sensitivity. In addition, V_{SOC} shows a negligible decrease after continuously operating for 2000 circles, presenting excellent robustness. Thus, in the future,

the rationally patterned MAS can make a difference to the development of VR/AR (virtual/augmented reality), sports training, smart home and smart city.

IV. MATERIALS AND METHODS

A. FABRICATION OF THE MAS

The fabrication process of the MAS can be divided into the preparation of the acrylic bone, the electrode layers, the conductive channels and the triboelectric layers. A hollow hemisphere with diameter of 30 mm and thickness of 1 mm was cut by a precision machine tool to form the bottom acrylic substrate with height of 2 mm, outer diameter of 17.2 mm and inner diameter of 15.2 mm. Then, four lead wire holes with diameter of 0.8 mm were fabricated by laser cutting technique, after which a Kapton film was pasted on the bottom acrylic substrate to act as a mask. The mask was patterned by a laser cutter, on which copper paste was brushed uniformly. Four one eighth ring shaped electrodes were obtained with outer diameter of 10 mm and inner diameter of 7 mm. A PTFE film was pasted on the electrodes after removing the mask. As for the middle section of the MAS, a ring-shaped acrylic plate with outer diameter of 17.2 mm and inner diameter of 15.2 mm was obtained by cutting an acrylic plate with thickness of 2 mm. A stainless-steel ball with diameter of 3 mm selected as the moving part of the MAS. With respect to the top section, an acrylic sheet with thickness of 1mm was cut into a disk with diameter of 17.2 mm and its following fabrication process was the same as the bottom section. For the assembling process, the acrylic plates were firmly connected with each other by the Loctite 414.

B. MEASUREMENTS OF THE MAS

The MAS was mounted on a linear motor (LinMot BF01-37) and the moving distance and acceleration can be controlled by the linear motor. The V_{OC} and V_{SOC} were directly tested by a LabVIEW testing system, consisting of a data acquisition card (NI USB-6356), a LabVIEW testing program, and a PC.

REFERENCES

[1] F. Landreani and E. G. Caiani, "Smartphone accelerometers for the detection of heart rate," *Expert Rev. Med. Devices*, vol. 14, no. 12, pp. 935–948, 2017.

[2] S. Finkbeiner, "MEMS for automotive and consumer electronics," in *Proc. IEEE Int. Solid-State Circuits Conf.*, 2003, pp. 9–14.

[3] M. Xu *et al.*, "A soft and robust spring based triboelectric nanogenerator for harvesting arbitrary directional vibration energy and self-powered vibration sensing," *Adv. Energy Mater.*, vol. 8, no. 9, 2018, Art. no. 1702432.

[4] W. Babatain, S. Bhattacharjee, A. M. Hussain, and M. M. Hussain, "Acceleration sensors: Sensing mechanisms, emerging fabrication strategies, materials, and applications," *ACS Appl. Electron. Mater.*, vol. 3, no. 2, pp. 504–531, 2021.

[5] H. Zhang, X. Wei, Y. Ding, Z. Jiang, and J. Ren, "A low noise capacitive MEMS accelerometer with anti-spring structure," *Sens. Actuator A. Phys.*, vol. 296, pp. 79–86, 2019.

[6] N. Gupta *et al.*, "Design and fabrication of SOI technology based MEMS differential capacitive accelerometer structure," *J. Mater. Sci. Technol.*, vol. 30, no. 16, pp. 15705–15714, 2019.

[7] X. Fan *et al.*, "Graphene ribbons with suspended masses as transducers in ultra-small nanoelectromechanical accelerometers," *Nat. Electron.*, vol. 2, no. 9, pp. 394–404, 2019.

[8] B. Jo, H. Takahashi, T. Takahata, and I. Shimoyama, "Highly sensitive angular accelerometer utilizing piezoresistive cantilever and spiral liquid channel," in *Proc. IEEE 32th Int. Conf. Micro Electro Mech. Syst.*, 2019, pp. 206–209.

[9] D. N. Li, Q. Q. Fan, J. H. Li, and W. Ren, "Design and analysis of a novel mems piezoelectric accelerometer for vector hydrophone," in *Proc. 13th Symp. Piezoelectrcity Acoustic Waves Device Appl.*, 2019, pp. 1–6.

[10] D. Zhang, J. Liu, L. Qin, J. Liu, and M. Li, "Multiparameter modeling of piezoelectric six-degree-of-freedom accelerometer about sensitivity characteristics," *IEEE Sens. J.*, vol. 20, no. 13, pp. 7129–7137, Jul. 2020.

[11] Z. L. Wang, T. Jiang, and L. Xu, "Toward the blue energy dream by triboelectric nanogenerator networks," *Nano Energy*, vol. 39, pp. 9–23, 2017.

[12] C. Wu, A. C. Wang, W. Ding, H. Guo, and Z. L. Wang, "Triboelectric nanogenerator: A foundation of the energy for the new era," *Adv. Energy Mater.*, vol. 9, no. 1, 2019, Art. no. 1802906.

[13] H. Guo *et al.*, "A highly efficient triboelectric negative air ion generator," *Nat. Sustain.*, vol. 4, no. 2, pp. 147–153, 2020.

[14] W. Xu *et al.*, "A droplet-based electricity generator with high instantaneous power density," *Nature*, vol. 578, no. 7795, pp. 392–396, 2020.

[15] Z. Wu, H. Guo, W. Ding, Y. - C. Wang, L. Zhang, and Z. L. Wang, "A hybridized triboelectric–electromagnetic water wave energy harvester based on a magnetic sphere," *ACS Nano*, vol. 13, no. 2, pp. 2349–2356, 2019.

[16] K. Dong *et al.*, "A stretchable yarn embedded triboelectric nanogenerator as electronic skin for biomechanical energy harvesting and multifunctional pressure sensing," *Adv. Mater.*, vol. 30, no. 43, 2018, Art. no. e1804944.

[17] Z. Wu *et al.*, "Highly durable and easily integrable triboelectric foam for active sensing and energy harvesting applications," *Adv. Mater. Technol.*, vol. 6, no. 1, 2020, Art. no. 2000737.

[18] Q. F. Shi, T. Y. Y. He, and C. Lee, "More than energy harvesting - Combining triboelectric nanogenerator and flexible electronics technology for enabling novel micro-/nano-systems," *Nano Energy*, vol. 57, pp. 851–871, 2019.

[19] B. Zhang *et al.*, "All-in-one 3D acceleration sensor based on coded liquid–metal triboelectric nanogenerator for vehicle restraint system," *Mater. Today*, vol. 43, pp. 37–44, 2021.

[20] X. J. Pu *et al.*, "Eye motion triggered self-powered mechnosensational communication system using triboelectric nanogenerator," *Sci. Adv.*, vol. 3, no. 7, 2017, Art. no. e1700694.

[21] Z. Wu, B. Zhang, H. Zou, Z. Lin, G. Liu, and Z. L. Wang, "Multifunctional sensor based on translational-rotary triboelectric nanogenerator," *Adv. Energy Mater.*, vol. 9, no. 33, 2019, Art. no. 1901124.

[22] Z. Wu, T. Cheng, and Z. L. Wang, "Self-powered sensors and systems based on nanogenerators," *Sensors*, vol. 20, no. 10, 2020, Art. no. 2925.

[23] H. Y. Guo *et al.*, "A highly sensitive, self-powered triboelectric auditory sensor for social robotics and hearing aids," *Sci. Robot.*, vol. 3, no. 20, 2018, Art. no. 9.

[24] Q. Shi *et al.*, "Deep learning enabled smart mats as a scalable floor monitoring system," *Nat. Commun.*, vol. 11, no. 1, 2020, Art. no. 4609.

[25] T. Chen *et al.*, "Novel augmented reality interface using a self-powered triboelectric based virtual reality 3D-control sensor," *Nano Energy*, vol. 51, pp. 162–172, 2018.

[26] J. Chen *et al.*, "Enhancing performance of triboelectric nanogenerator by filling high dielectric nanoparticles into sponge PDMS film," *ACS Appl. Mater. Interfaces*, vol. 8, no. 1, pp. 736–744, 2016.

[27] L. Chen, Q. Shi, Y. Sun, T. Nguyen, C. Lee, and S. Soh, "Controlling surface charge generated by contact electrification: Strategies and applications," *Adv. Mater.*, vol. 30, no. 47, 2018, Art. no. 1802405.

[28] K. H. Koh *et al.*, "A self-powered 3D activity inertial sensor using hybrid sensing mechanisms," *Nano Energy*, vol. 56, pp. 651–661, 2019.

[29] T. Bhatta, P. Maharjan, M. Salauddin, M. T. Rahman, S. S. Rana, and J. Y. Park, "A battery-less arbitrary motion sensing system using magnetic repulsion-based self-powered motion sensors and hybrid nanogenerator," *Adv. Funct. Mater.*, vol. 30, no. 36, 2020, Art. no. 2003276.

[30] Z. Wang, F. Zhang, N. Li, T. Yao, D. Lv, and G. Cao, "Self-powered multifunctional triboelectric sensor based on PTFE/PU for linear, rotary, and vibration motion sensing," *Adv. Mater. Technol.*, vol. 5, no. 7, 2020, Art. no. 2000159.

[31] Y. K. Pang, X. H. Li, M. X. Chen, C. B. Han, C. Zhang, and Z. L. Wang, "Triboelectric nanogenerators as a self-powered 3D acceleration sensor," *ACS Appl. Mater. Interfaces*, vol. 7, no. 34, pp. 19076–19082, 2015.

[32] M. Shi *et al.*, "Self-powered analogue smart skin," *ACS Nano*, vol. 10, no. 4, pp. 4083–4091, 2016.

[33] H. Zou *et al.*, "Quantifying the triboelectric series," *Nat. Commun.*, vol. 10, no. 1, 2019, Art. no. 1427.

[34] F. Caiazzo, F. Curcio, G. Daurelio, and F. Memola Capece Minutolo, "Laser cutting of different polymeric plastics (PE, PP and PC) by a CO_2 laser beam," *J. Mater. Process. Technol.*, vol. 159, no. 3, pp. 279–285, 2005.

BAOCHENG WANG was born in Weifang, China. He received the B.Eng. degree in polymer material and engineering from the Qingdao University of Science and Technology, Qingdao, China, in 2020. He is currently working toward the M.Sc. degree in nano science and technology with the Beijing Institute of Nanoenergy and Nanosystems, Chinese Academy of Sciences, Beijing, China. His current research interests include self-powered sensors and systems based on nanogenerators.

XUELIAN WEI was born in Lanzhou, China. She received the M.Sc. degree in materials science and engineering from the China University of Mining and Technology (CUMT), Xuzhou, China, in 2020. She is currently working toward the Ph.D. degree in nano science and technology with the Beijing Institute of Nanoenergy and Nanosystems, Chinese Academy of Sciences, Beijing, China. Her current research interests include triboelectric nanogenerator based energy harvesting and self-powered sensing systems.

JUNHUAN CHEN was born in Zhoukou, China. She received the B.Sc. degree in applied chemistry from Shenyang Ligong University, Shenyang, China, in 2019. She is currently working toward the M.Sc. degree in marine corrosion and protection with the Institute of Oceanology, Chinese Academy of Sciences, Qingdao, China. Her current research interests include triboelectric nanogenerators for energy harvesting.

ZHIHAO YUAN was born in Shanghai. He received the B.Sc. degree in applied physis from the Shanghai University of Electric Power, Shanghai, China, in 2018. He is currently working toward the M.Sc. degree in condensed state physics with Guangxi University, Nanning, China. His current research interests include self-powered sensors and systems based on nanogenerators.

YAPENG SHI was born in Pingdingshan, China. He received the B.Eng. degree in polymer material and engineering from the Tianjin University of Science and Technology, Tianjin, China, in 2019. He is currently working toward the M.Sc. degree in physical chemistry with the Beijing Institute of Nanoenergy and Nanosystems, Chinese Academy of Sciences, Beijing, China. His current research interests include triboelectric nanogenerator, self-powered electronic skin.

ZHIYI WU received the Ph.D. degree in instrument science and technology from Chongqing University, Chongqing, China, in 2013. He is currently working toward a Researcher with the Beijing Institute of Nanoenergy and Nanosystems, Chinese Academy of Sciences. His current research interests include nanoenergy and self-powered sensors. His research studies have been published in top-notch journals, including *Advanced Material, Advanced Energy Materials, Materials Today, Nano Energy, ACS Nano, Applied Physics Letters*, etc.

ZHONG LIN WANG is a Hightower Chair and Regents's Professor with Georgia Tech. He is also the Chief Scientist and Director for the Beijing Institute of Nanoenergy and Nanosystems, Chinese Academy of Sciences. His discovery and break-throughs in developing nanogenerators establish the principle and technological road map for harvesting mechanical energy from environmental and biological systems for powering personal electronics. He coined and pioneered the field of piezotronics and piezo-phototronics by introducing piezoelectric potential gated charge transport process in fabricating new electronic and optoelectronic devices.